

Article

# Catalysts for Methane Steam Reforming Reaction: Evaluation of CeO<sub>2</sub> Addition to Alumina-Based Washcoat Slurry Formulation

Vincenzo Palma , Eugenio Meloni , Simona Renda  and Marco Martino \* 

Department of Industrial Engineering, University of Salerno, Via Giovanni Paolo II 132,  
84084 Fisciano (SA), Italy; vpalma@unisa.it (V.P.); emeloni@unisa.it (E.M.); srenda@unisa.it (S.R.)

\* Correspondence: mamartino@unisa.it; Tel.: +39-089-969275

Received: 29 June 2020; Accepted: 31 July 2020; Published: 3 August 2020



**Abstract:** The effect of the addition of CeO<sub>2</sub> to alumina-based washcoat slurry formulation on the methane steam reforming (MSR) reaction was investigated. Five Al<sub>2</sub>O<sub>3</sub>-CeO<sub>2</sub>-based washcoat slurries, differing from each other in the Al<sub>2</sub>O<sub>3</sub>/CeO<sub>2</sub> ratio (nominal ratio equal to ∞, 0.042, 0.087, 0.250, 0.667) were prepared, dried and calcined; the resulting powders were loaded with nickel as an active metal and the obtained catalysts were tested in MSR reaction. Five cylindrical silicon carbide (SiC) monoliths were washcoated with the prepared slurries and their mechanical resistance was evaluated through the ultrasound adherence test. The activity tests results highlighted the best performance in terms of methane conversion and hydrogen selectivity of the powder catalyst, with the Al<sub>2</sub>O<sub>3</sub>/CeO<sub>2</sub> percentage nominal ratio equal to 0.042. A structured catalyst was finally prepared by loading a SiC monolith with the most active catalytic formulation and tested in MSR reaction. The performance of the structured catalyst was evaluated in terms of methane conversion and its stability was verified in a time-on-stream test, which allowed for the evaluation of the carbon formation rate; furthermore, its activity was characterized by the estimation of the kinetic parameters. The results highlighted the beneficial effect of ceria addition on the catalytic activity; moreover, compared with data of the literature, the calculated carbon formation rate demonstrated a good resistance of the catalyst to coke formation.

**Keywords:** methane steam reforming; structured catalysts; nickel; ceria; kinetics

## 1. Introduction

The idea of hydrogen as the next-generation energy carrier has widely spread in the last years, mainly because of the growing concerns related to environmental pollution, in particular greenhouse gasses emissions, which are strictly connected to fossil fuel combustion for power generation and automotive applications [1,2]. Methane steam reforming (MSR) is, to date, the most consolidated technology in hydrogen production [3,4]. The process is based on both the homonymous and the water gas shift (WGS) reactions, reported in Equations (1) and (2), which are a highly endothermic and a slightly exothermic equilibrium reaction, respectively.



The MSR reaction needs a huge amount of energy in order to occur with the desirable extent: it is conventionally performed in furnace reactors, in which heat is provided at the external wall of each catalyst containing tubes by combustion [5]. Heat supply to the catalytic bed is actually the limiting aspect in the reforming process: heat transport resistances typical of this process cause the generation of temperature gradients from the external tube wall to the axial position inside the catalytic bed, thus requiring very high temperatures outside the tubes [6]. This is mainly due to the fact that, in conventional catalysts, active metals are usually supported on metal oxides, which are non-conductive materials. This leads to a drastic decrease in the temperature in radial direction, from the wall to the center of the reactor since heat transport resistances occurs. In this perspective, process intensification of MSR mainly deals with the optimization of thermal management in reforming systems. Several solutions have been proposed, involving the change from a fixed bed configuration to the fluidized bed one [7], or from the heat supply from external firing to direct heating, such as with microwaves [8]. Another attractive solution is represented by the microchannel reactor, which can enhance the heat transfer to the reaction zone [9,10]. Furthermore, catalysis-related solutions have been proposed, generally concerning the application of high conductive structured catalysts, which, thanks to their better heat transfer properties and their peculiar structures, offer the possibility of flattening the thermal profile both in radial and axial directions [11]. In previous works, cordierite and silicon carbide (SiC) monoliths have been investigated for the MSR reaction both in wall-flow and flow-through configuration, showing very promising results [12,13], as well as FeCr-alloy monoliths [14]. The flattening of the thermal profile allows the decrease in the temperature gradient. In particular, this means that the desired temperature at the center of the catalytic bed can be reached with lower external temperatures [3]. Moreover, a monolith structured catalyst allows one to avoid some undesired effects, such as channeling or blocking, which are typical issues in powder- and/or pellet-fixed beds [15]. In structured catalysts, usually the monolith acts as a carrier, so a dedicated catalytic formulation composed of both the support and the active metals needs to be deposited and stabilized on the structure. The choice of the most suitable formulation is generally performed through a screening of powder catalysts and, once the better performing one is individuated, the selected formulation can be transferred to the structured carrier. With the aim of achieving a well-performing structured catalyst, some other aspects have to be taken in consideration in the powder catalyst preparation, such as the adhesion to the carrier surface, which mainly deals with the support properties and of course depends on the operating conditions of temperature and pressure. The most consolidated technology for structured catalyst preparation is the deposition of a washcoat on the surface, and then the loading of the active metal. Washcoats are generally alumina-based materials, because of the excellent alumina properties of resistance to high temperatures and remarkably high specific surface area, which enhances several catalytic processes [16,17]. Catalyst doping is a widely diffuse methodology in order to improve the performances of the MSR in terms of activity and selectivity, as well as to have more stable catalysts, which can resist sintering and coke deactivation [18–20]. In the last years, the interest towards rare earth oxides applications in catalysis has rapidly spread, and they have been widely applied as support dopants. Boudjeloud et al. [21] recently reported that the addition of La to  $\alpha$ -Al<sub>2</sub>O<sub>3</sub> in Ni-based catalysts for methane steam reforming causes strong changes at the surface of NiO sites, and the produced strong Ni-La-Al interactions determine a better dispersion of the active metal onto the support surface, resulting in smaller average Ni particle size and in a higher spacing between Ni particles, which prevents their agglomeration and thus sintering. Arandiyani et al. [22] studied the catalytic behavior of La<sub>0.4</sub>M<sub>0.6</sub>Al<sub>0.2</sub>Ni<sub>0.8</sub>O<sub>3</sub> perovskite-type oxides (where M corresponded to several noble metals) on carbon deposition, obtaining a very promising result in terms of resistance to coke deposition with Rh addition. Habibi et al. [23] investigated the effect of the MgO/Al<sub>2</sub>O<sub>3</sub> ratio in mesoporous nanocrystalline MgO Al<sub>2</sub>O<sub>3</sub> powders, and the study pointed out that the higher the ratio, the lower the reducibility of the prepared sample and the higher its basicity; for these characteristics, the sample with the higher MgO content showed the highest resistance to carbon formation. Sepehri et al. [24] evaluated the performance of several Ni/CeO<sub>2</sub> catalysts, obtaining that deactivation of the 20%Ni/CeO<sub>2</sub>

catalyst could be ascribed to Ni sintering rather than to carbon deposition. Similar results were achieved in other numerous studies reporting alumina doping, mainly with a small, fixed amount of lanthana or ceria, which can be considered the most promising doping agents for Ni/Al<sub>2</sub>O<sub>3</sub> catalysts in MSR reaction [25–29]. While the positive effect of ceria on Al<sub>2</sub>O<sub>3</sub>-CeO<sub>2</sub>-based catalysts for methane steam reforming has been discussed and clarified, the application of these formulations to structured catalysts and the evaluation of the catalytic performances in presence of Ni-based catalysts supported on Al<sub>2</sub>O<sub>3</sub>-CeO<sub>2</sub> washcoats for this application remains largely unexamined. For this reason, this work aimed to investigate MSR reaction in presence of several Al<sub>2</sub>O<sub>3</sub>-CeO<sub>2</sub> washcoat formulations with different Al<sub>2</sub>O<sub>3</sub>/CeO<sub>2</sub> ratios in order to identify the most active washcoat formulation to be used for the preparation of a structured catalyst. In the first part of this study, a screening of the prepared Ni/washcoat catalysts was performed, with samples in powder shape, obtained by drying and calcining the washcoat slurries. The desired amount of Ni was deposited via wet impregnation method. Once identified the better catalyst, in the second part of this work the selected formulation was transferred on a SiC monolith: the structured catalyst was obtained by washcoating the monolith with the chosen slurry, and subsequently Ni was loaded via wet impregnation in the nickel salt precursor solution. The performances of the structured catalyst were evaluated in terms of activity towards the methane steam reforming reaction and carbon formation rate. Moreover, the kinetic parameters were determined based on the results of dedicated reaction tests.

## 2. Materials and Methods

### 2.1. Washcoat Slurries Preparation

The washcoat slurries were prepared by mixing, under mechanical stirring, commercial ceria powder (Opaline; Actalys HAS; Rhodia, Milano, Italy) with a colloidal solution, obtained by acidification (pH = 4 by nitric acid) of a suspension of pseudoboehmite (Pural SB; Sasol, Milano, Italy) in a solution at 1 wt % of methyl cellulose (Viscosity 4000 cP; SigmaAldrich, Milano, Italy). For reference, one slurry was prepared without adding ceria. In summary, five washcoat slurries were prepared based on the Al<sub>2</sub>O<sub>3</sub>/CeO<sub>2</sub> percentage nominal ratio equal to ∞, 0.042, 0.087, 0.250, 0.667 and they were denoted as *x*AlCe where *x* corresponds to Al<sub>2</sub>O<sub>3</sub> weight percentage in the support. The main chemical–physical characteristics of the commercial ceria and pseudoboehmite are reported in Table 1.

**Table 1.** Chemical–physical characteristics of commercial ceria and pseudoboehmite.

Chemical	SSA (B.E.T.) (m <sup>2</sup> /g)	Crystallite Size (nm)		Particle Size D50 (μm)	Impurities (%)
		CeO <sub>2</sub> (111)	Al <sub>2</sub> O <sub>3</sub> (120)		
Actalys HAS	246	6.1	-	0.041–20	La <sub>2</sub> O <sub>3</sub> (≤0.1); Pr <sub>6</sub> O <sub>11</sub> (≤0.1); Nd <sub>2</sub> O <sub>3</sub> (≤0.1)
Pural SB	250	-	5.0	45	Na <sub>2</sub> O (0.002)

### 2.2. Catalysts Preparation

The powder catalysts were prepared via wet impregnation, with an aqueous solution of nickel acetate tetrahydrate (99.998% trace metals basis, Sigma Aldrich, Milano, Italy), of powder supports obtained by drying and calcining the washcoat slurries at 850 °C, for 3 h. The nickel loading was ≈5 wt %. Five SiC monoliths of 30 mm of length and 18 mm of diameter were washcoated by dip-coating procedure [30]; the monoliths were dipped in the slurries (based on the Al<sub>2</sub>O<sub>3</sub>/CeO<sub>2</sub> percentage nominal ratio equal to 0.042, 0.087, 0.250, 0.667, ∞) for 30 min and the excess was removed by centrifuge at 3000 rpm with a CWS 4236 centrifuge (Biotecnica s.a.s., Napoli, Italy). The dip-coating procedure was repeated four times until reaching a loading ≈15 wt %, and after each cycle they were dried at 120 °C for 3 h and calcined at 850 °C for 1h. Subsequently, the SiC monolith washcoated with the slurry based on the Al<sub>2</sub>O<sub>3</sub>/CeO<sub>2</sub> percentage nominal ratio equal to 0.042 was impregnated with

nickel acetate tetrahydrate (99.998% trace metals basis, Sigma Aldrich) to obtain a nickel loading of  $\approx 5$  wt %, with respect to the coating weight.

### 2.3. Catalysts Characterization

A series of physical–chemical analytical techniques were used to fully characterize the catalysts. The ultrasound adherence tests were performed on washcoated monolith samples by immersing them in a beaker containing 100 mL of ethanol with a CP104 (EIA S.p.A, Arezzo, Italy) filled with distilled water over six cycles of five minutes. The specific surface areas measurements were carried out by dynamic  $N_2$  adsorption at 77 K with a Costech Sorptometer 1040 (Costech International, Milano, Italy). The XRD diffractograms were obtained with a D8 Advance (Bruker, Milano, Italy) using a Cu Ka radiation source (35 kV; 40 mA) in the  $2\theta$  range (20–80) (Stp = 737; Stp size = 0.0814; t/Stp = 0.5 s). Moreover the crystallite sizes were calculated by applying the Scherrer equation. The Hg porosimetry technique (by using “PASCAL 140” and “PASCAL 240” instruments, Thermo Finnigan Instruments, Brescia, Italy) was used for the determination of both the average pore diameter and pores distribution in the prepared SiC samples. The chemical composition was determined by ARL<sup>TM</sup> QUANT’X ED-XRF spectrometer (Thermo Scientific, Rodano, Italy). The Raman spectra were obtained by using an inVia Raman Microscope (Renishaw, Pianezza, Italy), equipped with a 514 nm Ar ion laser operating at 25 mW. Scanning electron microscope (SEM) images were obtained by a field emission scanning electron microscope (FE-SEM, mod. LEO 1525, Carl Zeiss SMT AG, Oberkochen, Germany) coupled to an energy dispersive X-ray analyzer (EDX mod. INCA Energy 350, Oxford Instruments, Abingdon, UK).

### 2.4. Catalytic Activity Tests

Before the catalytic activity tests, the powder catalysts were compressed and sieved in order to obtain a particle distribution in the 180–355  $\mu\text{m}$  range. The activity tests were carried out by loading the samples in a stainless-steel tubular reactor, located horizontally in a heated furnace; channeling and entrainment phenomena were avoided by hindering the powder between two quartz wool disks. The catalyst was diluted with quartz glass spheres with the same size in a 1:1 volumetric ratio (total volume  $\approx 7$  mL). Before each the activity test, the catalysts were reduced in hydrogen by feeding a 500 Ncc/min of a mixture 5 vol %  $H_2$  in Ar from 20  $^\circ\text{C}$  to 850  $^\circ\text{C}$  with a ramp of 5  $^\circ\text{C}/\text{min}$ . The activity tests were carried out at atmospheric pressure, in the temperature range 500–850  $^\circ\text{C}$ , at a weight hourly space velocity (WHSV) = 15.8 mL/g·h, with a steam to methane ratio = 3. The structured catalyst was surrounded by a thermo expanding pad with a thickness of 2 mm, previously reduced at the same conditions of the powder catalysts. The activity tests were carried out in a stainless-steel tubular reactor (internal diameter = 22 mm, length = 400 mm) at atmospheric pressure in the temperature range 500–850  $^\circ\text{C}$  at a WHSV = 15.8 mL/g·h (the same as the powder catalysts). For both powder and structured catalysts activity tests, the product gas stream composition was analyzed on dry basis, by condensing the water by means of a refrigerator Julabo F12 (Seelbach, Germany); the anhydrous product stream was sent to a Hiden Analytical mass spectrometer (Hiden Analytical, 420 Europa Blvd, Westbrook, Warrington WA5 7 UN, UK). The catalytic performances were evaluated in terms of methane conversion ( $X_{CH_4}$ ) and hydrogen yield ( $Y_{H_2}$ ), as expressed in Equations (3) and (4), respectively; the carbon formation rate (CFR) was calculated as reported in Equation (5).

$$X_{CH_4} = \frac{\text{mol}_{CH_4,in} - \text{mol}_{CH_4,out}}{\text{mol}_{CH_4,in}} \quad (3)$$

$$Y_{H_2} = \frac{\text{mol}_{H_2,out}}{4 \cdot \text{mol}_{CH_4,in}} \quad (4)$$

$$\text{CFR} = \frac{\text{mass}_{\text{coke}}}{\text{mass}_{\text{catalyst}} \cdot \text{mass}_{\text{carbon, fed}} \cdot \text{time}} \cdot 100 \quad (5)$$

### 2.5. Kinetic Measurements

The model parameters were obtained through the numerical analysis of the results of dedicated experimental tests, performed as described in the previous paragraph, in the temperature range 550–850 °C. In particular, in order to assume differential reaction conditions with negligible heat and mass transfer effects, the data regarding the catalytic performance of the system far from the thermodynamic equilibrium conditions were considered for developing the model.

For the numerical analysis, MSR and WGS reactions (respectively Equations (1) and (2)) were supposed to occur and the reaction rates considered to estimate the kinetic parameters were expressed by Equation (6) for the former and Equation (7) for the latter. The reaction rate expression follows the approach proposed by Haberman and Young [31].

MSR

$$-r_{SR} = k_{SR} \left( P_{CH_4} P_{H_2O} - \frac{P_{H_2}^3 P_{CO}}{K_{eq,SR}} \right) \quad (6)$$

WGS

$$-r_{WGS} = k_{WGS} \left( P_{CO} P_{H_2O} - \frac{P_{CO_2} P_{H_2}}{k_{eq,WGS}} \right) \quad (7)$$

Arrhenius expression

$$k_i = k_{0,i} e^{-\frac{E_{a,i}}{RT}} \quad (8)$$

In the above reported expressions,  $P_i$  is the partial pressure of the “ $i$ ” component, while  $k_i$  is the reaction rate constant, according to the Arrhenius law (Equation (8)), where the parameters  $k_{0,i}$  and  $E_{a,i}$  correspond respectively to the pre-exponential factor and to the activation energy. The equilibrium constants of the two reactions are expressed as Equation (9) for MSR and Equation (10) for WGS, and Equation (11).

$$K_{eq,SR} = 1.0267 \times 10^{10} \cdot \exp(-0.2513 \cdot Z^4 + 0.3665 \cdot Z^3 + 0.5810 \cdot Z^2 - 27.134 \cdot Z + 3.2770) [Pa^2] \quad (9)$$

$$K_{eq,WGS} = \exp(-0.2935 \cdot Z^3 + 0.6351 \cdot Z^2 + 4.1788 \cdot Z + 0.3169) \quad (10)$$

$$Z = \frac{1000}{T [K]} - 1 \quad (11)$$

The material balances on the single components led to the obtainment of a set of equations, solved by applying the Euler method by means of the Excel software. For each operating condition, the experimental value  $x_{exp}$  and the corresponding kinetic model solution  $x_{mod}$  were compared, and an objective function was defined as Equation (12). The minimization of the objective function (through the Solver of the Excel software) leaving the kinetic parameters ( $E_{a,i}$  and  $k_{0,i}$ ) as degrees of freedom for the solution allowed the achievement of very close experimental and modelled values. The optimization procedure was performed several times with various initial values of the parameters, with the aim of confirming the robustness of the optimization scheme.

$$f = \min \left( \sum_{c=1}^n (x_{exp_c} - x_{mod_c})^2 \right) \quad (12)$$

### 3. Results and Discussion

The supports used in the preparation of the powder catalysts were obtained by drying and calcining a series of slurries at 850 °C that are hypothetically usable in structured catalysts preparation, with the aim of selecting the most promising catalytic formulation. Two aspects were previously investigated: the mechanical resistance of the coating obtained by washcoating SiC monoliths, and the catalytic activity of the chemical formulations.

### 3.1. Characterization Results

It is a consolidated opinion that a series of parameters might influence the quality of the coating in  $\text{Al}_2\text{O}_3$ -washcoated structures, such as the alumina particle size [32] or the  $\text{HNO}_3/\text{Al}_2\text{O}_3$  and  $\text{H}_2\text{O}/\text{Al}_2\text{O}_3$  ratios [33]. More complex is the role that each parameter has in mixed washcoat slurries, in which is not the alumina but another oxide, such as ceria, to be dispersed in the colloidal solution of the alumina primer. In these cases, not only the adherence of the coating on structure is affected by the presence of the dispersed oxide, but also the catalytic activity is affected by the presence of two or more chemical supports. Four cylindrical SiC monolithic samples (30 mm in length and 18 mm in diameter) were washcoated with the precursor slurries of 4AlCe, 8AlCe, 20AlCe and 40AlCe (Table 2) following the same procedure used for the preparation of the structured catalyst as described in the Section 3.2, and exposed to the ultrasound adherence test [34]. For reference, a cylindrical SiC monolith was washcoated with the slurry prepared without adding ceria (Al\_SiC). The results (Figure 1) clearly suggested a correlation between the alumina loading and the weight loss.

**Table 2.** Characterization of powder supports.

Sample	$\text{Al}_2\text{O}_3/\text{CeO}_2$ (Nominal Ratio)	Composition (wt %)		SSA (B.E.T.) ( $\text{m}^2/\text{g}$ )
		CeO <sub>2</sub>	Al <sub>2</sub> O <sub>3</sub>	
4AlCe	0.042	96.2	4.0	65
8AlCe	0.087	92.1	7.9	68
20AlCe	0.250	80.9	18.7	75
40AlCe	0.667	61.8	37.2	92
$\gamma$ -Al <sub>2</sub> O <sub>3</sub>	$\infty$	-	100	140

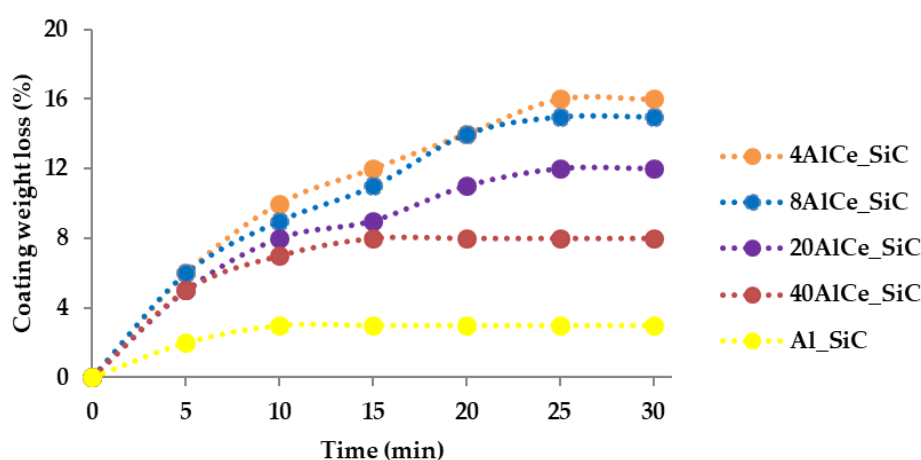


**Figure 1.** Comparison of the coating weight losses of five washcoated SiC monoliths in the ultrasound adherence test.

Of course, better mechanical properties are desirable in structured catalysts, and would suggest the individuation of 40AlCe-SiC as the most suitable washcoat formulation for this application. However, the resistance to the mechanical stress [35] is only one of the parameters affecting the choice of the ideal slurry for the preparation of the structured catalyst; the composition of the slurry is even more important than the mechanical properties in the choice of the catalytic formulation. The ED-XRF analysis showed the composition of the powder supports obtained from the slurries (Table 2), and the nickel loading in the powder catalysts (Table 3).

The specific surface area measurements showed an increase in specific surface area with the increase in the alumina content of the powder supports, and this is clearly related to the higher surface area of  $\gamma$ -Al<sub>2</sub>O<sub>3</sub> rather than CeO<sub>2</sub>. Moreover, a decrease in the SSA was observed in each catalyst if compared to its bare support, due both to the nickel loading, which might occlude some porosities,

and to the additional calcination step (Table 3). The crystallite sizes of the catalysts were also calculated by means of the Scherrer equation [36] on the CeO<sub>2</sub> plains (111), showing no substantial differences between the catalysts (Table 3).

**Table 3.** Characterization of powder catalysts.

Sample	Ni loading (wt %)	SSA (B.E.T.) (m <sup>2</sup> /g)	Crystallite Size–CeO <sub>2</sub> (111) (nm)
Ni4AlCe	4.7	60	6.1
Ni8AlCe	4.9	61	6.3
Ni20AlCe	4.7	69	6.2
Ni40AlCe	4.7	86	6.4
NiAl <sub>2</sub> O <sub>3</sub>	4.9	125	-

The XRD diffractograms showed almost exclusively the typical ceria face-centered cubic fluorite-type crystal phase in all the catalysts obtained by impregnation of the ceria-based supports [37], however, in the case of Ni20AlCe and Ni40AlCe, some  $\gamma$ -alumina peaks were also visible in the background (Figure 2). No peaks corresponding to the NiO phase were detected, probably due to a good dispersion and to the detection limit of the instrument.

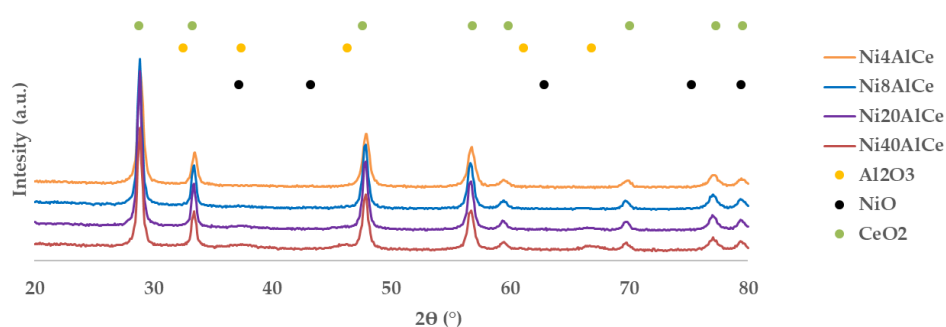


**Figure 2.** XRD diffractograms of the powder catalysts.

The Raman spectra obtained for the most relevant ceria-based powder catalysts and the ceria used in the washcoat slurries preparation showed the typical strong peak at 464 cm<sup>-1</sup>, attributed to the first order F<sub>2g</sub> mode [38], corresponding to the Ce<sup>4+</sup>-O-Ce<sup>4+</sup> wagging (Figure 3a), and some barely visible broad bands between 550 and 700 cm<sup>-1</sup> attributed to the defect-induced (D) band and NiOx stretching modes (Figure 3b). It is well known that the ceria D band consists of two peaks at 560 and 600 cm<sup>-1</sup>, which are respectively attributed to defects and to the Ce<sup>3+</sup>-O-Ce<sup>4+</sup> stretching mode [39] (Figure 3b).

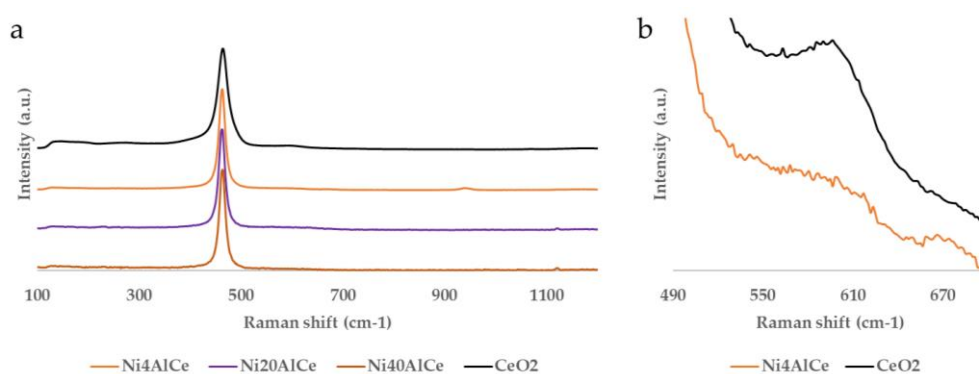


**Figure 3.** Raman spectra of the Ni4AlCe, Ni20AlCe and Ni40AlCe powder catalysts and of the ceria powder used in the washcoat slurries preparation (a), and the comparison between Ni4AlCe and ceria in the defect zone (b).

The weak Raman band of NiO supported on  $\gamma$ -Al<sub>2</sub>O<sub>3</sub> was described to be located at 550 cm<sup>-1</sup> [40]; moreover, two main Raman active transitions at 566 and 640 cm<sup>-1</sup> were reported and assigned to the presence of NiO on ceria [41]. In the case of Ni<sub>x</sub>AlCe powder catalysts, an overlapping between the ceria D band and the Ni-O stretching modes may have occurred, thus, it was not possible to differentiate the bands or evaluate the oxygen defect concentration for ceria-based catalysts. However, the spectra showed no significant effect of alumina on the ceria-typical transitions.

The H<sub>2</sub>-TPR profiles of the NiAl<sub>2</sub>O<sub>3</sub> catalyst showed a broad peak centered in the temperature range of 500 to 550 °C (Figure 4), which was attributed to the reduction in nickel oxides interacting with the alumina surface. Moreover, a broad peak near 800 °C was attributed to nickel aluminate [42]. More complex is the case of the ceria-based catalysts, in which four main broad peak were identified; the peak, centered at  $\approx$ 300 °C, was attributed to the reduction in nickel oxide interacting with the ceria surface, while the shoulder at  $\approx$ 500 °C was attributed to the nickel oxide interacting with the alumina surface. A broad peak at  $\approx$ 350 °C was attributed to ceria surface reduction, while at  $\approx$ 800 °C a possible overlapping between the nickel aluminate and ceria bulk reduction may occur [43].

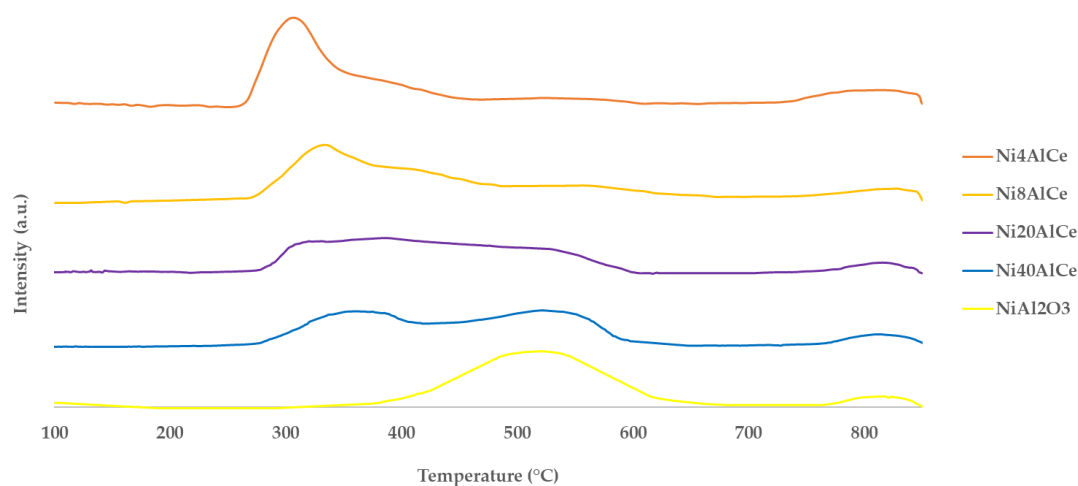


**Figure 4.** H<sub>2</sub>-TPR profiles of the Ni<sub>4</sub>AlCe, Ni<sub>8</sub>AlCe, Ni<sub>20</sub>AlCe and Ni<sub>40</sub>AlCe and NiAl<sub>2</sub>O<sub>3</sub> powder catalysts.

As shown below, the results of the catalytic activity tests performed on the powder catalysts showed an increase in activity of the powder catalysts with the increase in ceria content, and highlighted the best performance of the Ni<sub>4</sub>AlCe catalyst. On the other hand, the ultrasound adherence test showed an opposite trend in the stability of the coating, which improved with the increase in the alumina content. Since the differences in stability were limited to 7–8% in weight loss, the Ni<sub>4</sub>AlCe was selected as the preferential formulation to be transferred to the structured carrier.

The effect of the washcoat and active species deposition on the bare SiC carrier was also evaluated by means of the Hg porosimetry technique. The results are shown in Figure 5 in terms of distribution of the pores vs. pore size. The results shown in Figure 5 evidenced that the average pore size of the bare SiC monolith (blue curve) is higher than that of the samples with only the washcoat (green curve) and washcoat + Ni (red curve). By deeply analyzing Figure 5, it is possible to argue that the washcoat, as well the active species deposition, besides the decrease in the pore diameter, had a beneficial effect on the pore distribution since the related curves are tighter than the one of the bare SiC, thus resulting in a more homogeneous pore sizes. Moreover, the smaller porosities with a diameter smaller than 5  $\mu$ m, which are clearly absent in the bare SiC sample, are evident for the green and red curves, and this further confirms that the deposition of the washcoat and active species created new porosities and a consequent rougher surface in the catalytic samples. This is reflected in the increased surface area with respect to the bare SiC carrier, as shown in Table 4.

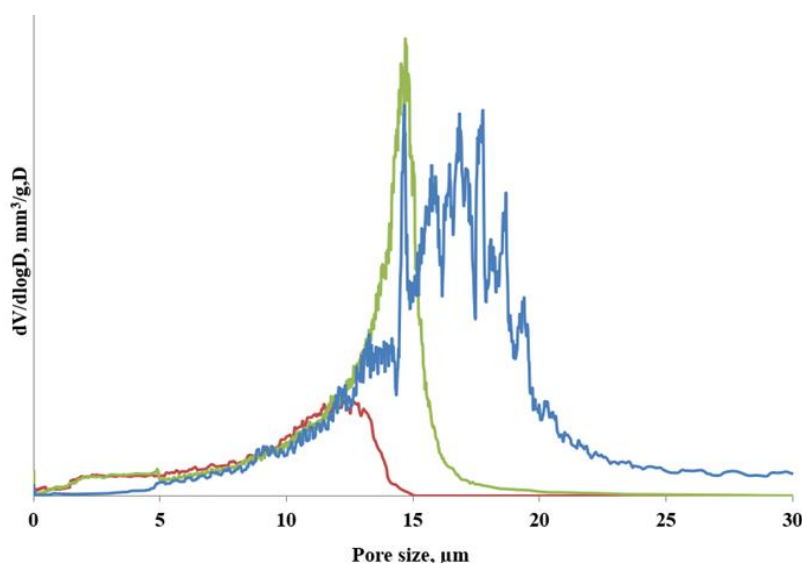


**Figure 5.** Porosimetry distribution of the different SiC samples used in this work: bare SiC (blue curve), 4AlCe-SiC (green curve), Ni4AlCe-SiC (red curve).

**Table 4.** Characterization of structured catalyst.

Sample	Loading (wt %)		SSA (B.E.T.) (m <sup>2</sup> /g)	Average Pore Diameter (μm)	Carbon Formation Rate (mg <sub>coke</sub> /g <sub>cat</sub> ·g <sub>C,fed</sub> ·h)
	Ni	Coating (4AlCe)			
Bare SiC	-	-	0.35	17	-
4AlCe-SiC	-	-	12	14	-
Ni4AlCe-SiC	0.77	15.12	11	9	-
Ni4AlCe-SiC_spent	0.75	14.90	7	7.5	0.35

The SEM images at various magnitudes related to the final prepared catalyst are shown in Figure 6. The images highlighted that the inner porosities of the SiC monolith are not plugged after the washcoat and active species deposition (Figure 6a,b). Moreover, the homogeneous deposition on the SiC granules is evident (Figure 6c). In addition, the decrease in the average diameter of the inner porosities from 17 to 9 μm shown in Figure 5 is confirmed by SEM images.

In Figure 6d the cross section of Ni4AlCe-SiC\_spent catalyst is shown. The sample was obtained by cutting the structured catalyst transversely with a workshop saw. As can be seen, the addition of the washcoat layer changes the shape of the SiC channel, which becomes quite circular; moreover, in this case it becomes difficult to define a layer thickness, as it is thicker on the corners of the SiC channels, and narrows moving from the corner towards the center of the wall. However, an average thickness of 200 μm was estimated.

The distribution of elements on the final catalytic sample (Ni4AlCe-SiC), obtained by EDX element mapping (Figure 7), highlights how the active species (Ni) and the washcoat (Ce and Al) cover all the SiC granules, confirming the particularly good and homogeneous dispersion obtained with the preparation procedure.

The main textural properties of the spent monolithic catalysts, in comparison with those of the as-prepared catalysts, are reported in Table 4, in which also the carbon formation rate is presented.

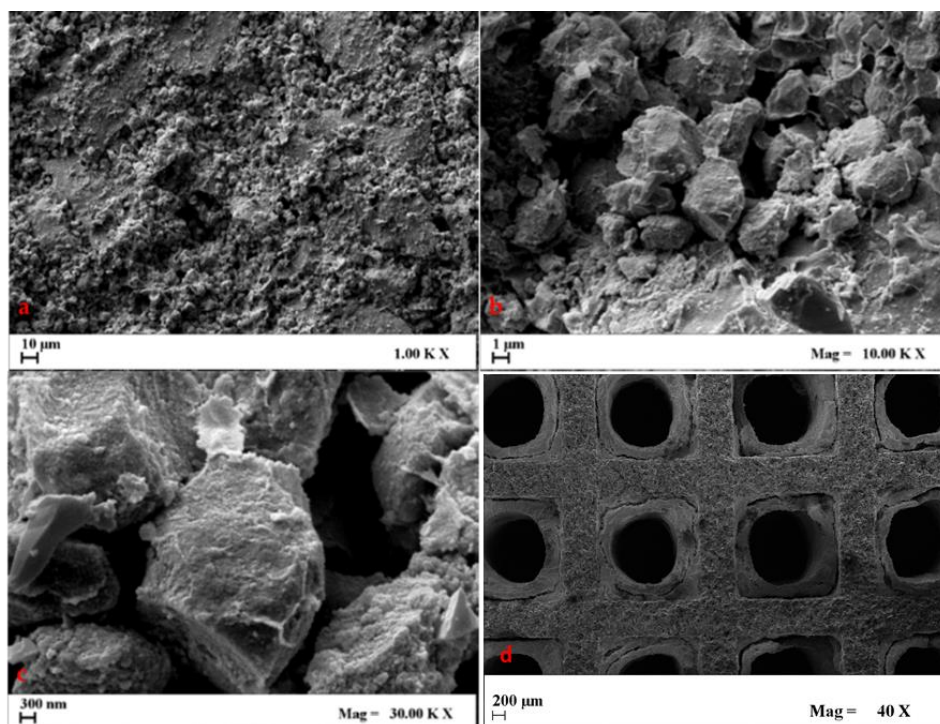


**Figure 6.** SEM images at various magnitudes for the final catalytic monolith Ni<sub>4</sub>AlCe-SiC (a–c); SEM image of the cross section of Ni<sub>4</sub>AlCe-SiC\_spent (d).

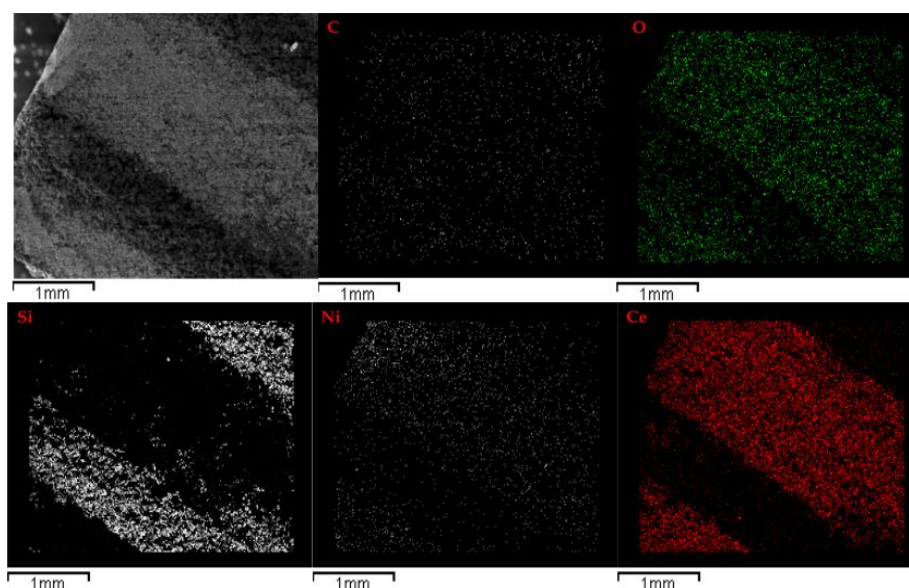


**Figure 7.** SEM image and distribution of elements, as obtained by energy dispersive X-ray (EDX) element mapping, for the final catalytic monolith Ni<sub>4</sub>AlCe-SiC.

The ED-XRF analysis, carried out on the fresh catalyst (Ni<sub>4</sub>AlCe-SiC) and the spent structured catalyst (Ni<sub>4</sub>AlCe-SiC\_spent), showed a decrease in the washcoat loading, which was attributed to a slight exfoliation of the layer, probably due the thermal effects. As evident, the SSA of the catalyst decreased after the catalytic test, as well as the average pore diameter, due to the carbon deposition on the surface and in the porosities of the structure. A dedicated temperature-programmed oxidation (TPO) test was performed for the evaluation of the carbon deposited on the structured catalyst following the stability tests shown in the next section. The CFR, which indicates the average

coking rate (the amount of carbon deposited per gram of catalyst and per hour) is lower than that reported in the literature for analogous catalysts [28], thus confirming the good performance of the prepared sample also in this sense. The two peaks present in the CO and CO<sub>2</sub> curves at temperatures higher than 500 °C (Figure 8) suggested the deposition of two types of carbon on the catalyst surface during the MSR stability test (specifically, filamentous and graphitic carbon), which resulted in the catalyst deactivation [44].

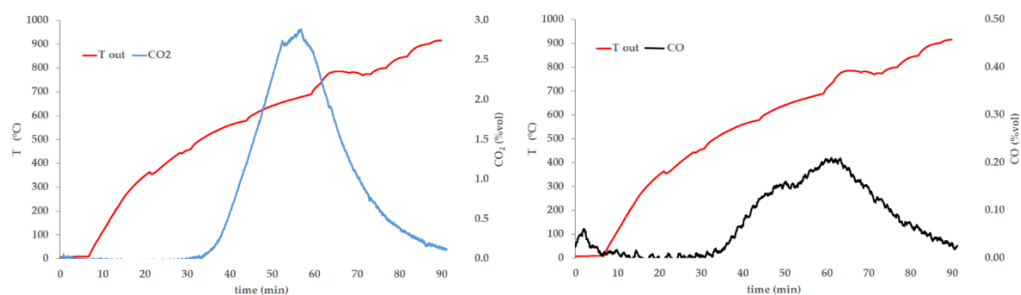


**Figure 8.** CO<sub>2</sub> (left) and CO (right) profiles during a temperature-programmed oxidation (TPO) test performed with the structured catalysts after a methane steam reforming (MSR) stability test.

### 3.2. Activity Tests Results

The catalytic activity tests performed on the powder catalysts under the operating conditions illustrated in Section 3.4 are discussed in this section. A first result of the screening of the formulations, in terms of CH<sub>4</sub> conversion trend, is reported in Figure 9. The dependence of the methane conversion on the ceria content in the support is clearly highlighted: the higher the CeO<sub>2</sub> loading, the higher the conversion values in the whole investigated temperature range. Despite the high space velocity, the catalyst in which the 96 wt % of the support was ceria (Ni4AlCe) approached the equilibrium conversion at 830 °C and was still active under 500 °C (Figure 9). On the other hand, the pure alumina-supported catalyst (NiAl<sub>2</sub>O<sub>3</sub>) showed an almost negligible activity above 750 °C. The hydrogen yield follows the same CH<sub>4</sub> conversion trend for each sample, thus demonstrating the good selectivity of all the catalysts. The variation in the H<sub>2</sub>/CO<sub>2</sub> and H<sub>2</sub>/CO molar ratios was evaluated in order to estimate the extent of both WGS and MSR reactions. Figure 10 displays the values of the two ratios obtained under different operating temperatures and their theoretical values obtained from the thermodynamic analysis of the reaction system. The thermodynamic trend can be explained by the two competitive reactions, reported in Equations (1) and (2), and the extent to which they are integrated into the system. Thus, it is possible to distinguish four limit cases, as listed in Table 5.

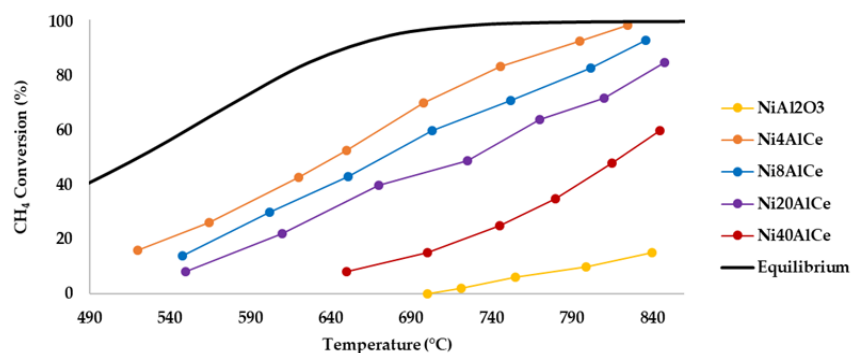


**Figure 9.** CH<sub>4</sub> conversion as function of the temperature; comparison between the powder catalysts (weight hourly space velocity (WHSV) = 15.8 mL/g·h; H<sub>2</sub>O/CH<sub>4</sub> = 3).

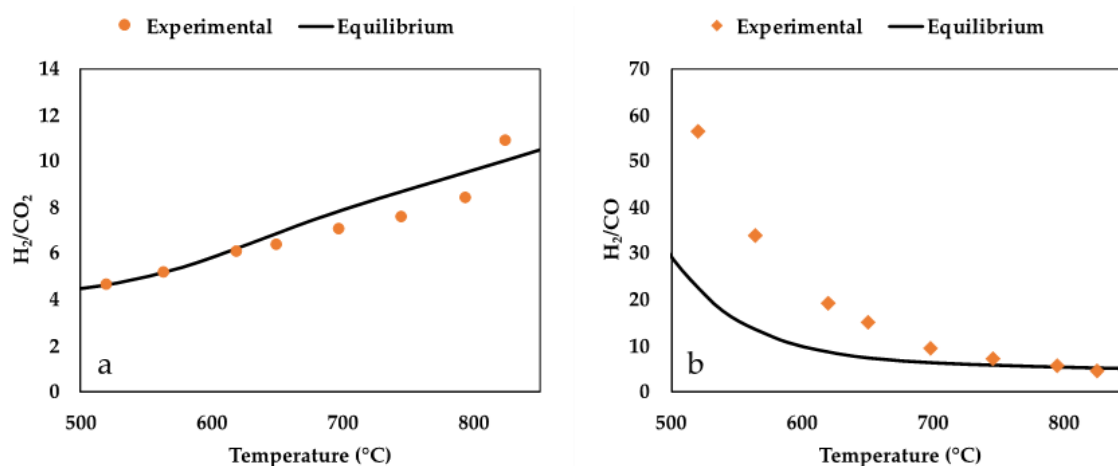


**Figure 10.**  $H_2/CO_2$  (a) and  $H_2/CO$  (b) ratios for the Ni4AlCe powder catalyst (WHSV = 15.8 mL/g·h;  $H_2O/CH_4 = 3$ ).

**Table 5.** Thermodynamic  $H_2/CO_2$  and  $H_2/CO$  ratios.

a	$X_{MSR} \rightarrow 0$ and $X_{WGS} \rightarrow 0$	$H_2/CO \rightarrow 3$ $H_2/CO_2 \rightarrow 4$
b	$X_{MSR} \rightarrow 0$ and $X_{WGS} \rightarrow 100$	$H_2/CO \rightarrow \infty$ $H_2/CO_2 \rightarrow 4$
c	$X_{MSR} \rightarrow 100$ and $X_{WGS} \rightarrow 100$	$H_2/CO \rightarrow \infty$ $H_2/CO_2 \rightarrow 4$
d	$X_{MSR} \rightarrow 100$ and $X_{WGS} \rightarrow 0$	$H_2/CO \rightarrow 3$ $H_2/CO_2 \rightarrow \infty$

Since MSR is an endothermic reaction and WGS is an exothermic reaction, cases (a) and (c) are not likely to occur. Case (b) is thermodynamically promoted at low temperatures, while case (d) is favored by high temperatures. With respect to these considerations, it is possible to observe from Figure 8 that, at low temperatures, the experimental  $H_2/CO_2$  ratio reaches the threshold value of 4, while the experimental  $H_2/CO$  ratio is remarkably higher than its equilibrium value. This means that, below 600 °C, CO conversion through WGS reaches the equilibrium extent.

The methane conversion reported in Figure 9 seems to support this allegation since its value is far from the equilibrium, but  $H_2/CO_2$  is almost 4, meaning that the produced CO is almost completely converted to  $CO_2$  and the ratio of  $H_2/CO$  is higher than the equilibrium (Figure 10).

$H_2/CO_2$  is very close to the equilibrium value in the whole temperature range, while at 810 °C the opposite condition is obtained: the  $H_2/CO$  ratio reaches the equilibrium value according to the methane conversion, but the temperature is too high for WGS to still be at its equilibrium condition. Indeed, the  $H_2/CO_2$  ratio is now higher than the equilibrium, as only a fraction of the produced CO is converted into  $CO_2$ .

As previously stated, because Ni4AlCe gave the highest  $CH_4$  conversion with an almost 100% selectivity to hydrogen, it was selected as the most promising formulation to be transferred to the structured catalyst.

The results of the activity tests performed by using the structured catalysts are shown in Figure 11 in terms of  $CH_4$  conversion and  $CO_2$  concentration (on dry base) vs. temperature.

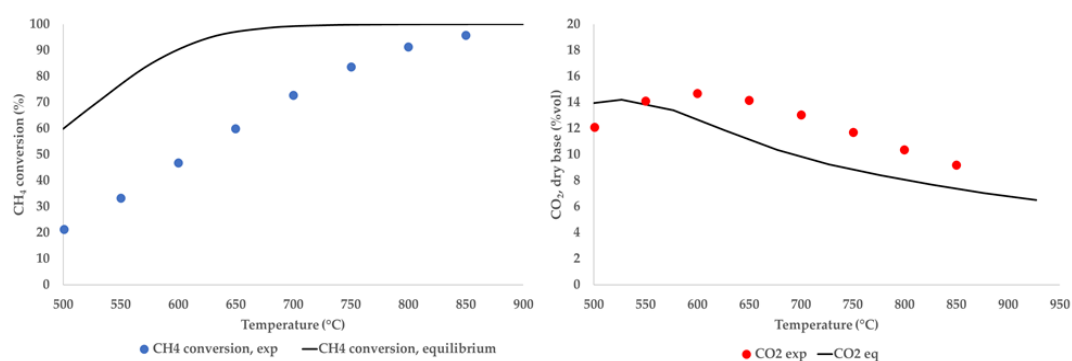


**Figure 11.** CH<sub>4</sub> conversion (left) and CO<sub>2</sub> concentration (right) vs. temperature for the structured catalyst (WHSV = 15.8 mL/g·h; H<sub>2</sub>O/CH<sub>4</sub> = 3).

The results shown in Figure 11 highlight a good activity of the structured catalyst towards the methane steam reforming, since a CH<sub>4</sub> conversion closer to that of the thermodynamic equilibrium is evident at about 850 °C, with no differences with respect to the powder formulation (Figure 9). Moreover, the CO<sub>2</sub> concentration exceeding that of the equilibrium in the investigated range denoted an appreciable activity of this catalyst towards the water gas shift (WGS) reaction, as also observed for the corresponding powder sample. Similar behavior of Ni/CeO<sub>2</sub>-based catalysts has not yet been observed in the literature, thus confirming the affinity of this kind of catalyst towards WGS [45].

The catalyst stability was evaluated by performing stability tests at a fixed temperature for 50 h. The temperature for the test was fixed at 600 °C in order to establish a condition in which the catalyst still has a good activity but, at the same time, coke formation is promoted; the result in terms of CH<sub>4</sub> conversion vs. time is shown in Figure 12.

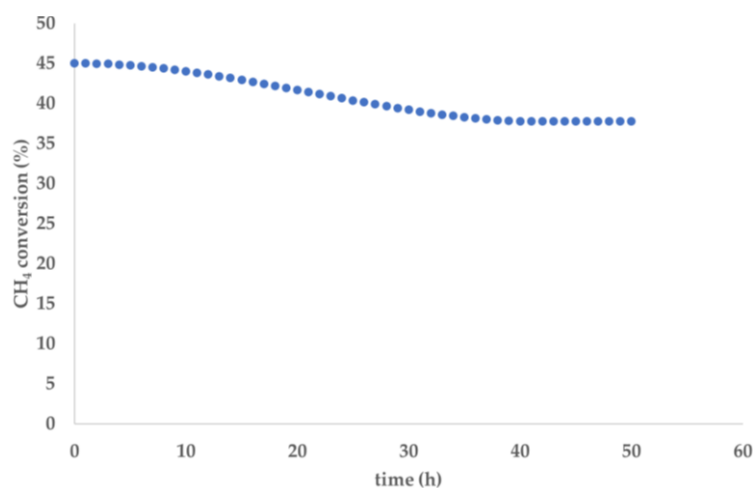


**Figure 12.** CH<sub>4</sub> conversion vs. time for a stability test of 50 h at 600 °C (WHSV = 15.8 mL/g·h; H<sub>2</sub>O/CH<sub>4</sub> = 3).

The stability test performed at 600 °C displayed a decrease in CH<sub>4</sub> conversion from 45% to about 37% after 50 h of time on stream, thus denoting the tendency of this catalyst to deactivate at low temperature due to coke formation (Table 4). Nevertheless, the conversion values highlighted a decrease in the slope of the CH<sub>4</sub> conversion curve, thus indicating that an equilibrium condition between the coke formation and its gasification was reached. No coke formation was registered at temperatures higher than 700 °C.

### 3.3. Discussion

The catalytic activity tests result of the powder catalysts and the good coke resistance of Ni<sub>4</sub>AlCe-SiC-structured catalyst were attributed to the promotional effect of the ceria support. In powder catalysts, the presence of ceria decreased the reduction temperature of nickel oxide; in fact the H<sub>2</sub>-TPR profiles showed a temperature reduction onset below 300 °C in the case of the Ni<sub>4</sub>AlCe sample, while in the case of the NiAl<sub>2</sub>O<sub>3</sub> one, the reduction began over 350 °C. The improved reducibility greatly affected the methane conversion, which increased with the ceria content at the same temperature. The Ni<sub>4</sub>AlCe catalysts approached the equilibrium conversion at ≈820 °C and were still active at 500 °C; on the other hand, NiAl<sub>2</sub>O<sub>3</sub> showed no methane conversion below 700 °C and an almost negligible activity at 850 °C. The decrease in specific surface area with the increase in ceria content, in the powder catalysts, did not seem to depress the catalytic activity; on the contrary, the worst conversion of methane was obtained with the NiAl<sub>2</sub>O<sub>3</sub> catalysts, which showed the highest specific surface area, while the highest methane conversion was obtained with Ni<sub>4</sub>AlCe, which showed the lowest specific surface area among the powder catalysts. Ceria has been reported to have a beneficial effect on coke resistance as well; the data reported in this article confirm this effect, showing a lower carbon formation rate than those reported in the literature for similar catalytic systems. In fact, ceria-based catalysts, due to their oxygen transfer capacity, are able to disfavor the carbon deposition by promoting the gasification of carbon deposits [42].

### 3.4. Kinetic Measurements

The kinetic parameters, namely, the pre-exponential factor and activation energy, for the developed model are reported in Table 6.

**Table 6.** Kinetic parameters for the structured catalyst.

	$k_0$	$E_a$ (kJ/mol)
Steam reforming	856 mol/g·min·atm <sup>2</sup>	71
Water gas shift	11,190 mol/g·min	33

The model fitting of the experimental data is shown in Figure 13, where the product stream composition experimentally evaluated through the mass spectrometer analysis is compared to the composition resulting from the developed model.

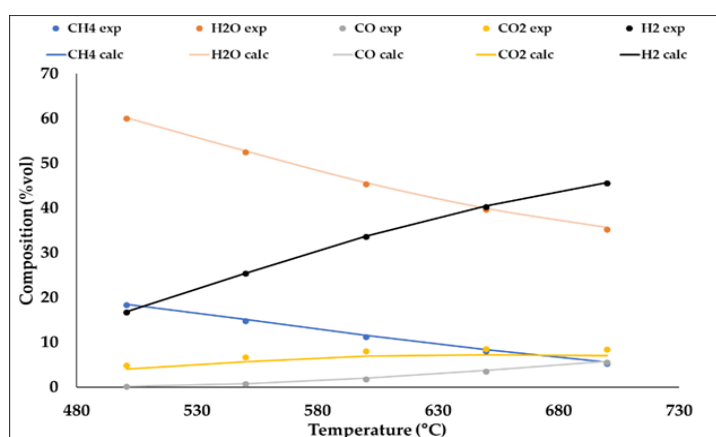


**Figure 13.** Comparison of the experimental and kinetic model results for the structured catalyst (WHSV = 15.8 mL/g·h; H<sub>2</sub>O/CH<sub>4</sub> = 3).

The data showed a good agreement between the modelled and the experimental values in the investigated temperature range, thus proving the feasibility of the developed kinetic model.

In particular, the model is able to describe the above-discussed good extent of WGS reaction in the presence of this structured catalyst (Figure 11). The calculated activation energy for the steam reforming reaction (about 71 kJ/mol) is lower than that reported in the literature for the Ni-based commercial catalysts (about 96 kJ/mol) [46], thus confirming the good performance of the prepared catalyst.

#### 4. Conclusions

In this article the effect of the addition of ceria to an alumina-based washcoat was evaluated, both in terms of catalytic activity and the mechanical resistance of the corresponding washcoated SiC monoliths. Five washcoat slurries were prepared based on different  $\text{Al}_2\text{O}_3/\text{CeO}_2$  percentage ratios equal to 0.042, 0.087, 0.250, 0.667; part of each slurry was dried and calcined in order to obtain the corresponding powder supports, which were loaded with the active metal (5 wt % Ni), while the remaining part of the slurry was used to washcoat five cylindrical shaped SiC monoliths. The MSR catalytic activity tests showed that the  $\text{CH}_4$  conversion increased with the ceria content, while, on the contrary, the ultrasound adherence test showed a decrease in the mechanical resistance on the washcoat layer with the increase in ceria content. The catalytic activity of the powder catalysts was related to the reducibility; the ceria addition in fact reduced the temperature reduction on NiO, thus providing a beneficial effect on the performance of the catalyst. Finally, the washcoated monolith, with the  $\text{Al}_2\text{O}_3/\text{CeO}_2$  percentage nominal ratio equal to 0.042, was loaded with the active metal (5 wt % Ni with respect to the washcoat layer weight) and tested in the methane steam reforming reaction to estimate the kinetic parameters. The carbon formation rate after a certain amount of time in the stream test was also estimated, with the results showing a good resistance to coke formation. The obtained carbon formation rate was lower than those reported in the literature for similar catalytic systems, suggesting a promotional effect of ceria that is able to disfavor the carbon deposition by promoting the gasification of carbon deposits.

**Author Contributions:** All authors equally contributed to the conceptualization, methodology, software, validation, formal analysis, investigation, resources, data curation, writing-original draft preparation, writing-review and editing, visualization, supervision, project administration and funding acquisition of this manuscript. All authors have read and agreed to the published version of the manuscript.

**Funding:** This research received no external funding.

**Acknowledgments:** The authors wish to thankfully acknowledge Roberto Clerici (Sasol Performance Chemicals) for providing the alumina used in this work. The authors wish to thankfully acknowledge Mariarosa Scognamiglio (Department of Industrial Engineering, University of Salerno) for SEM analysis.

**Conflicts of Interest:** The authors declare no conflict of interest.

#### References

1. Bhat, S.A.; Sadhukhan, J. Process Intensification Aspects for Steam Methane Reforming: An Overview. *AIChE J.* **2009**, *55*, 408–422. [[CrossRef](#)]
2. Angeli, S.D.; Turchetti, L.; Monteleone, G.; Lemonidou, A. Catalyst development for steam reforming of methane and model biogas at low temperature. *Appl. Catal. B Environ.* **2016**, *181*, 34–46. [[CrossRef](#)]
3. Meloni, E.; Martino, M.; Palma, V. A Short Review on Ni Based Catalysts and Related Engineering Issues for Methane Steam Reforming. *Catalysts* **2020**, *10*, 352. [[CrossRef](#)]
4. Castro-Dominguez, B.; Mardilovich, I.P.; Ma, L.C.; Ma, R.; Dixon, A.G.; Kazantzis, N.K.; Ma, Y.H. Integration of Methane Steam Reforming and Water Gas Shift Reaction in a Pd/Au/Pd-Based Catalytic Membrane Reactor for Process Intensification. *Membranes* **2016**, *6*, 44. [[CrossRef](#)]
5. Gallucci, F.; Paturzo, L.; Basile, A. A simulation study of the steam reforming of methane in a dense tubular membrane reactor. *Int. J. Hydrogen Energy* **2004**, *29*, 611–617. [[CrossRef](#)]
6. Palma, V.; Ricca, A.; Martino, M.; Meloni, E. Innovative structured catalytic systems for methane steam reforming intensification. *Chem. Eng. Process.* **2017**, *120*, 207–215. [[CrossRef](#)]

7. Marquez-Ruiz, A.; Wu, J.; Özkan, L.; Gallucci, F.; Van Sint Annaland, M. Optimal Operation and Control of Fluidized Bed Membrane Reactors for Steam Methane Reforming. *Comput. Aided Chem. Eng.* **2019**, *46*, 1231–1236. [[CrossRef](#)]
8. Palma, V.; Barba, D.; Cortese, M.; Martino, M.; Renda, S.; Meloni, E. Microwaves and Heterogeneous Catalysis: A Review on Selected Catalytic Processes. *Catalysts* **2020**, *10*, 246. [[CrossRef](#)]
9. Arzamendi, G.; Diéguez, P.M.; Montes, M.; Odriozola, J.A.; Falabella Sousa-Aguilar, E.; Gandía, L.M. Methane steam reforming in a microchannel reactor for GTL intensification: A computational fluid dynamics simulation study. *Chem. Eng. J.* **2009**, *154*, 168–173. [[CrossRef](#)]
10. Mbodji, M.; Commenge, J.M.; Falk, L.; Di Marco, D.; Rossignol, F.; Prost, L.; Valentin, S.; Joly, R.; Del-Gallo, P. Steam methane reforming reaction process intensification by using a millistructured reactor: Experimental setup and model validation for global kinetic reaction rate estimation. *Chem. Eng. J.* **2012**, *207–208*, 871–884. [[CrossRef](#)]
11. Palma, V.; Martino, M.; Meloni, E.; Ricca, A. Novel structured catalysts configuration for intensification of steam reforming of methane. *Int. J. Hydrogen Energy* **2017**, *42*, 1629–1638. [[CrossRef](#)]
12. Palma, V.; Ricca, A.; Meloni, E.; Miccio, M.; Martino, M.; Ciambelli, P. Methane Steam Reforming Intensification: Experimental and Numerical Investigations on Monolithic Catalysts. *Chem. Eng. Trans.* **2015**, *43*, 919–924. [[CrossRef](#)]
13. Palma, V.; Ricca, A.; Martino, M.; Meloni, E. Innovative Catalytic Systems for Methane Steam Reforming Intensification. *Chem. Eng. Trans.* **2016**, *52*, 301–306. [[CrossRef](#)]
14. Katheria, S.; Deo, G.; Kunzru, D. Rh-Ni/MgAl<sub>2</sub>O<sub>4</sub> catalyst for steam reforming of methane: Effect of Rh doping, calcination temperature and its application on metal monoliths. *Appl. Catal. A Gen.* **2019**, *570*, 308–318. [[CrossRef](#)]
15. López, E.; Divins, N.J.; Anzola, A.; Schbib, S.; Borio, D.; Llorca, J. Ethanol steam reforming for hydrogen generation over structured catalysts. *Int. J. Hydrogen Energy* **2013**, *38*, 4418–4428. [[CrossRef](#)]
16. Zhou, T.; Li, L.; Cheng, J.; Hao, Z. Preparation of binary washcoat deposited on cordierite substrate for catalytic applications. *Ceram. Int.* **2010**, *36*, 529–534. [[CrossRef](#)]
17. Papavasiliou, A.; Tsetsekou, A.; Matsouka, V.; Konsolakis, M.; Yentekakis, I.V. An investigation of the role of Zr and La dopants into Ce<sub>1-x-y</sub>Zr<sub>x</sub>La<sub>y</sub>O<sub>8</sub> enriched  $\gamma$ -Al<sub>2</sub>O<sub>3</sub> TWC washcoats. *Appl. Catal. A Gen.* **2010**, *382*, 73–84. [[CrossRef](#)]
18. Parizotto, N.V.; Rocha, K.O.; Damyanova, S.; Passos, F.B.; Zanchet, D.; Marques, C.M.P.; Bueno, J.M.C. Alumina-supported Ni catalysts modified with silver for the steam reforming of methane: Effect of Ag on the control of coke formation. *Appl. Catal. A Gen.* **2007**, *330*, 12–22. [[CrossRef](#)]
19. Rakass, S.; Oudghiri-Hassani, H.; Rowntree, P.; Abatzoglou, N. Steam reforming of methane over unsupported nickel catalysts. *J. Power Sources* **2006**, *158*, 485–496. [[CrossRef](#)]
20. Liu, C.J.; Ye, J.; Jiang, J.; Pan, Y. Progresses in the Preparation of Coke Resistant Ni-based Catalyst for Steam and CO<sub>2</sub> Reforming of Methane. *ChemCatChem* **2011**, *3*, 529–541. [[CrossRef](#)]
21. Boudjeloud, M.; Boulahouache, A.; Rabia, C.; Salhi, N. La-doped supported Ni catalysts for steam reforming of methane. *Int. J. Hydrogen Energy* **2019**, *44*, 9906–9913. [[CrossRef](#)]
22. Arandiyán, H.; Peng, Y.; Liu, C.; Chang, H.; Li, J. Effects of noble metals doped on mesoporous LaAlNi mixed oxide catalyst and identification of carbon deposit for reforming CH<sub>4</sub> with CO<sub>2</sub>. *J. Chem. Technol. Biotechnol.* **2013**, *89*, 372. [[CrossRef](#)]
23. Habibi, N.; Arandiyán, H.; Rezaei, M. Mesoporous MgOAl<sub>2</sub>O<sub>3</sub> nanopowder-supported meso–macroporous nickel catalysts: A new path to high-performance biogas reforming for syngas. *RSC Adv.* **2016**, *6*, 29576. [[CrossRef](#)]
24. Sepehri, S.; Rezaei, M.; Wang, Y.; Younesi, A.; Arandiyán, H. The evaluation of autothermal methane reforming for hydrogen production over Ni/CeO<sub>2</sub> catalysts. *Int. J. Hydrogen Energy* **2018**, *43*, 22340. [[CrossRef](#)]
25. Tribalis, A.; Panagiotou, G.D.; Bourikas, K.; Sygellou, L.; Kennou, S.; Ladas, S.; Lycourghiotis, A.; Kordulis, C. Ni Catalysts Supported on Modified Alumina for Diesel Steam Reforming. *Catalysts* **2016**, *6*, 11. [[CrossRef](#)]
26. El Doukkali, M.; Iriondo, A.; Arias, P.L.; Cambra, J.F.; Gandarias, I.; Barrio, V.L. Bioethanol/glycerol mixture steam reforming over Pt and PtNi supported on lanthana or ceria doped alumina catalysts. *Int. J. Hydrogen Energy* **2012**, *37*, 8298–8309. [[CrossRef](#)]
27. Yang, X.; Da, J.; Yu, H.; Wang, H. Characterization and performance evaluation of Ni-based catalysts with Ce promoter for methane and hydrocarbons steam reforming process. *Fuel* **2016**, *179*, 353–361. [[CrossRef](#)]

28. Dan, M.; Mihet, M.; Biris, A.R.; Marginean, P.; Almasan, V.; Borodi, G.; Watanabe, F.; Biris, A.S.; Lazar, M.D. Supported nickel catalysts for low temperature methane steam reforming: Comparison between metal additives and support modification. *React. Kinet. Mech. Catal.* **2012**, *105*, 173–193. [CrossRef]
29. Mortola, V.B.; Damyanova, S.; Zanchet, D.; Bueno, J.M.C. Surface and structural features of Pt/CeO<sub>2</sub>-La<sub>2</sub>O<sub>3</sub>-Al<sub>2</sub>O<sub>3</sub> catalysts for partial oxidation and steam reforming of methane. *Appl. Catal. B Environ.* **2011**, *107*, 221–236. [CrossRef]
30. Villegas, L.; Masset, F.; Guilhaume, N. Wet impregnation of alumina-washcoated monoliths: Effect of the drying procedure on Ni distribution and on autothermal reforming activity. *Appl. Catal. A Gen.* **2007**, *320*, 43–55. [CrossRef]
31. Haberman, B.A.; Young, J.B. Three-dimensional simulation of chemically reacting gas flows in the porous support structure of an integrated-planar solid oxide fuel cell. *Int. J. Heat Mass Transf.* **2004**, *47*, 3617–3629. [CrossRef]
32. Agrafiotis, C.; Tsetsekou, A. The effect of powder characteristics on washcoat quality. Part I: Alumina washcoats. *J. Eur. Ceram. Soc.* **2000**, *20*, 815–824. [CrossRef]
33. Valentini, M.; Groppi, G.; Cristiani, C.; Levi, M.; Tronconi, M.; Forzatti, P. The deposition of  $\gamma$ -Al<sub>2</sub>O<sub>3</sub> layers on ceramic and metallic supports for the preparation of structured catalysts. *Catal. Today* **2001**, *69*, 307–314. [CrossRef]
34. Yasaki, S.; Yoshino, Y.; Kazunori Ihara, D.; Ohkubo, K. Method of Manufacturing an Exhaust Gas Purifying Catalyst. U.S. Patent 5208206A, 4 May 1993.
35. Wua, D.; Zhang, Y.; Li, Y. Mechanical stability of monolithic catalysts: Improving washcoat adhesion by FeCrAl alloy substrate treatment. *J. Ind. Eng. Chem.* **2017**, *56*, 175–184. [CrossRef]
36. Holzwarth, U.; Gibson, N. The Scherrer equation versus the ‘Debye-Scherrer equation’. *Nat. Nanotechnol.* **2011**, *6*, 534. [CrossRef]
37. Phokha, S.; Pinitsoontorn, S.; Chirawatkul, P.; Poo-arporn, Y.; Maensiri, S. Synthesis, characterization, and magnetic properties of monodisperse CeO<sub>2</sub> nanospheres prepared by PVP-assisted hydrothermal method. *Nanoscale Res. Lett.* **2012**, *7*, 425. [CrossRef]
38. Cooper, A.; Davies, T.E.; Morgan, D.J.; Golunski, S.; Taylor, S.H. Influence of the Preparation Method of Ag-K/CeO<sub>2</sub>-ZrO<sub>2</sub>-Al<sub>2</sub>O<sub>3</sub> Catalysts on Their Structure and Activity for the Simultaneous Removal of Soot and NOx. *Catalysts* **2020**, *10*, 294. [CrossRef]
39. Xu, Y.; Wang, F.; Liu, X.; Liu, Y.; Luo, M.; Teng, B.; Fan, M.; Liu, X. Resolving a Decade-Long Question of Oxygen Defects in Raman Spectra of Ceria-Based Catalysts at Atomic Level. *J. Phys. Chem. C* **2019**, *123*, 18889–18894. [CrossRef]
40. Chan, S.S.; Wachs, I.E. In situ laser Raman spectroscopy of nickel oxide supported on  $\gamma$ -Al<sub>2</sub>O<sub>3</sub>. *J. Catal.* **1987**, *103*, 224–227. [CrossRef]
41. Murugan, R.; Vijayaprasath, G.; Mahalingam, T.; Ravi, G. Enhancement of room temperature ferromagnetic behavior of rf sputtered Ni-CeO<sub>2</sub> thin films. *Appl. Surf. Sci.* **2016**, *390*, 583–590. [CrossRef]
42. De Freitas Silva, T.; Costa Dias, J.A.; Guimarães Maciel, C.; Mansur Assaf, J. Ni/Al<sub>2</sub>O<sub>3</sub> catalysts: Effects of the promoters Ce, La and Zr on the methane steam and oxidative reforming reactions. *Catal. Sci. Technol.* **2013**, *3*, 635–643. [CrossRef]
43. Wang, L.; Liu, H.; Liu, Y.; Chen, Y.; Yang, S. Influence of preparation method on performance of Ni-CeO<sub>2</sub> catalysts for reverse water-gas shift reaction. *J. Rare Earths* **2013**, *31*, 559–564. [CrossRef]
44. Ginsburg, J.M.; Pina, J.; El Solh, T.; de Lasa, H.I. Coke Formation over a Nickel Catalyst under Methane Dry Reforming Conditions: Thermodynamic and Kinetic Models. *Ind. Eng. Chem. Res.* **2005**, *44*, 4846–4854. [CrossRef]
45. Kubacka, A.; Fernández-García, M.; Martínez-Arias, A. Catalytic hydrogen production through WGS or steam reforming of alcohols over Cu, Ni and Co catalysts. *Appl. Catal. A* **2016**, *518*, 2–17. [CrossRef]
46. Zeppieri, M.; Villa, P.L.; Verdone, N.; Scarsella, M.; De Filippis, P. Kinetic of methane steam reforming reaction over nickel- and rhodium-based catalysts. *Appl. Catal. A Gen.* **2010**, *387*, 147–154. [CrossRef]

